Modeling of Terahertz Heating Effects in Realistic Tissues

Sashikumaar Ganesan and Phaneendra K. Yalavarthy

Abstract—The terahertz (THz) propagation in real tissues causes heating as with any other electromagnetic radiation propagation. A finite-element (FE) model that provides numerical solutions to the heat conduction equation coupled with realistic models of tissues is employed in this study to compute the temperature raise due to THz propagation. The results indicate that the temperature raise is dependent on the tissue type and is highly localized. The developed FE model was validated through obtaining solutions for the steady-state case and showing that they were in good agreement with the analytical solutions. These types of models can also enable computation of specific absorption rates, which are very critical in planning/setting up experiments involving biological tissues.

Index Terms—Breast and brain, far infrared, finite element modeling, terahertz (THz) heating.

I. INTRODUCTION

TERAHERTZ (THz) technology advances in biomedical arena [1] have resulted in promising applications, including breast [2], [3], skin [4], and hard tissue imaging/spectroscopy [5]. The recent advances in THz time-domain spectroscopy (TDS) studies have made THz as one of the strong contenders for sensing and detection in defense applications [6], [7].

The THz uses far-infrared spectrum of wavelengths and is known to be a nonionizing type of radiation making it well suited for biomedical applications [1]–[5]. These THz systems are based on photoconductive switches that produce an average power of around 1μW. The modern THz systems use more powerful quantum cascade lasers or free electron lasers, which have the capabilities to produce the average power ranging from 1mW to 20 W [8]–[11]. These systems could cause permanent damage to the biological tissues under investigation when the exposure time is sufficiently large, compelling a detailed investigation of the THz exposure for better understanding of its effects. As with any other electromagnetic radiation interaction with tissue, the temperature distribution as a consequence of THz absorption is determined by the heat transfer mechanisms of conduction, convection, and radiation [12]. Determining such temperature elevation due to THz absorption is critical, as dielectric properties of tissues vary with temperature [12] and the detected THz signal is known to be sensitive to dielectric properties [13].

The heating effects of THz radiation in biological tissues have been investigated in the recent past [14], [15], with skin and water as case studies. These studies are inherently very useful in determining the heating effects and give first hand information about these; the models including the solutions were too simplistic to understand the transient behavior of heating effects. The work of Kristensen *et al.* [15] has assumed a static (steady-state) model and derived the analytical solution for Kirchoff's heat equation for the case of water. This study has motivated this work, where the transient behavior in realistic models consisting of different tissue types was considered here. The input parameters for the tissue types were identified from the literature. The realistic models here were both brain and breast models (see Figs. 1 and 2); as these are irregular geometries, a numerical scheme based on a finite-element method (FEM) was used to perform this study. This work also includes the investigation of showing that the FEM-based numerical scheme is in good agreement with the analytical solution proposed in [15]. As in the case of [15], the discussion here is limited to continuous-wave THz propagation with frequency of 1 THz and the specification of source is in terms of beam diameter and power (rather than power density).

Even though the realistic tissues that were considered here are only breast and brain models, the numerical scheme can be easily extended to other tissue models as well. The choice of FEM as the numerical method compared to others, such as finite difference, is due to flexibility offered by the FEM in terms of solving the partial differential equation (here, heat conduction equation) in irregular geometries.

As a part of this study, the finite-element (FE) mesh size and the THz beam spot diameter effect on the temperature raise were also studied along with transient behavior showing the dependence of temperature raise in the realistic models as a function of exposure time.

II. METHODS

A. Finite Element Modeling

Let the computational domain $\Omega \subset \mathbb{R}^3$, which may have several regions, be open and bounded. The heat transfer in Ω which is exposed to the THz radiation in the time interval $(0, I)$ is described by the heat conduction equation [12].
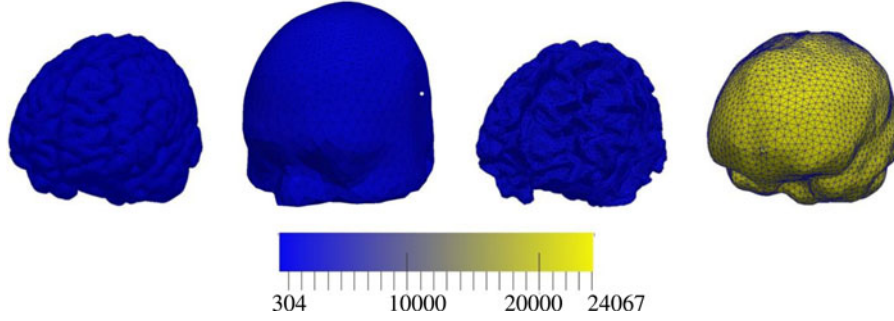
Fig. 1. Isosurfaces of different tissue types in the brain model, namely (left to right) gray matter, scalp/skull, white matter, and CSF layer. The color bar depicts the absorption coefficient (α in m^{-1}) for brain tissue types. The THz source location is specified as a white spot on the skull surface.
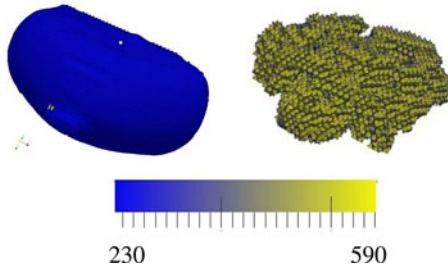

Fig. 2. Isosurfaces of the tissue types in the breast model used, namely (from left to right) fatty/adipose and fibroglandular tissue. The color bar depicts the absorption coefficient (α in m^{-1}) for breast tissue types. The THz source location is specified as a white spot on the fatty tissue surface.

$$\rho c_p \frac{\partial T}{\partial t} - \nabla \cdot (k\nabla T) = f \ \text{in} \quad \Omega \times (0, I)$$

$$T = T_0 \ \text{on} \quad \Gamma$$

$$k\nabla T \cdot n = 0 \ \text{on} \quad \partial\Omega \setminus \Gamma$$

$$T(\cdot, 0) = T_0 \ \text{in} \quad \Omega. \tag{1}$$

Here, $\rho(x, y, z)$ denotes the density (kg^{-3}), $c_p(x, y, z)$ the specific heat (JK^{-1}kg^{-1}), $k(x, y, z)$ the thermal conductivity (Wm^{-1}K^{-1}), $T(x, y, z, t)$ the temperature (K), t the time (s), I the given end time (s), Γ the Dirichlet part of the boundary $\partial\Omega$, and T_0 denotes the body temperature. Further, f is the dissipated power density, and in the z-direction it can be defined as follows. Let (x_p, y_p, z_p) on the surface $\partial\Omega$ be the center of the THz beam. We first transform the domain in the z-coordinate using the transformation $\hat{z} = z - z_p$, so that the center of the THz beam becomes $(x_p, y_p, 0)$. Now, we define the source term in the z-direction by

$$f = \begin{cases} \dfrac{\alpha P}{\pi a^2} \exp(-\alpha|\hat{z}|) & \text{for} \ 0 \leq r \leq a \\ 0 & \text{else} \end{cases}$$

where α is the absorption coefficient (m^{-1}), P the transmitted power (W), a the THz beam radius (m), and $r = \sqrt{(x - x_p)^2 + (y - y_p)^2}$. Note that the source in other coordinate directions can also be defined in a similar way.

In our model, we assume that the parameters ρ, c_p, and k are constants in each region of the domain, but may be different across the regions. We first transform the temperature using

the transformation $\hat{T} = T - T_0$ (indicating that our interest is only in computing the raise in temperature), and then scale the domain Ω with the characteristic length L to transform (1) into

$$\frac{\partial \hat{T}}{\partial t} - \frac{1}{\rho c_p L^2} \nabla \cdot (k\nabla\hat{T}) = \hat{f} \ \text{in} \ \hat{\Omega} \times (0, I)$$

$$\hat{T} = 0 \ \text{on} \ \hat{\Gamma}$$

$$k\nabla\hat{T} \cdot n = 0 \ \text{on} \ \partial\hat{\Omega} \setminus \hat{\Gamma}$$

$$\hat{T}(\cdot, 0) = 0 \ \text{in} \ \hat{\Omega} \tag{2}$$

where the transformed source term is given by

$$\hat{f} = \begin{cases} \dfrac{1}{\rho c_p} \dfrac{\alpha P}{\pi a^2} \exp(-\alpha|z|L) & \text{for} \ 0 \leq r \leq a \\ 0 & \text{else}. \end{cases} \tag{3}$$

Next, to solve the heat conduction equation by the FEM [16] we first derive the variational form. In order to impose the homogenous Dirichlet boundary condition in the ansatz and test spaces, we define $V = \{v \in H^1(\Omega) : v = 0 \ \text{on} \ \Gamma\}$, where $H^1(\Omega)$ is the usual Hilbert space. Now, we multiply the heat conduction equation (2) by a test function $v \in V$ and integrate it over Ω. After applying integration by parts to the second term in (2) and incorporating boundary conditions, the variational form becomes the following.

For given $f \in L^2((0, I] \times \Omega)$, find $\hat{T} \in L^2(0, I; V)$ with $T' \in L^2(0, I; V^{-1})$ such that

$$\left(\frac{\partial \hat{T}}{\partial t}, v\right) + \left(\frac{k}{\rho c_p L^2} \nabla\hat{T}, \nabla v\right) = \left(\hat{f}, v\right) \quad \forall v \in V. \tag{4}$$

Here, $(\cdot, \cdot)$ denotes the inner product in the Lebesque space $L^2(\Omega)$ and V^{-1} is the dual space of V.

Let $0 = t^0 < t^1 <, \ldots, t^N = I$ be the decomposition of the time interval $[0, I]$, and $\delta t = t^{n+1} - t^n$ be a uniform time step. Now, using the first-order, implicit backward Euler method the semidiscrete (in time) form of (4) in the time interval $(t^n, t^{n=1})$ can be written as follows.

For given T^n, find $T^{n+1} \in V$ such that

$$\left(\hat{T}^{n+1}, v\right) + \delta t \left(\frac{k}{\rho c_p L^2} \nabla\hat{T}^{n+1}, \nabla v\right)$$

$$= \delta t \left(\hat{f}^{n+1}, v\right) + \left(\hat{T}^n, v\right) \quad \forall v \in V.$$

TABLE 1
INPUT PARAMETERS FOR VARIOUS TISSUE TYPES IN THE
REALISTIC MODELS USED IN THIS STUDY

	ρ	c_p	k	α
water/CSF	997	3710	0.6064	24067
scalp and skull	1600	2000	0.3	327
gray matter	1030	3854	0.528	304
white matter	1030	3854	0.528	1000
fat	1100	4483	0.204	230
fibrous	1040	3500	0.518	590

The first four rows of the table correspond to the brain model used
and rest for breast model.

We triangulate the domain Ω into linear tetrahedra cells, and use the piecewise linear finite elements on each tetrahedron cell. Finally, we obtain the system of linear equations in the time interval (t^n, t^{n+1}) as [16]

$$(M + \delta t A) T^{n+1} = \delta t F^{n+1} + M T^n. \qquad (5)$$

Here, M and A are the mass and the stiffness matrices, respectively. Further, F is the load vector. The matrices and the load vector are assembled in parallel. In our parallel algorithm, we first decompose the collection of tetrahedra cells into N_P number of subcollection of cells using the package METIS [17], where N_P is the number of processors used in simulation. Then, we assemble the local matrices and load vector on each processor. Finally, we solve the algebraic system using the parallel solver MUMPS [18]. Note that the matrices and the load vector are independent of time. Thus, it is enough to assemble it only once at the start of the simulation. All computations were carried out on a Linux server with a 2.4-GHz 32-core AMD processor having 128-GB RAM.

B. Computational Models

We consider three different computational domains in this study. The first model is a cylindrical domain, which mimics the 3-D axisymmetric geometry used in [15], assumed to be filled with water. The radius and the height of the cylinder are 50 and 15 mm, respectively. Using the TetGen mesh generator [19], we triangulate the cylinder and obtain 23 666 vertices and 111 573 tetrahedral cells. This model is used to validate our FE scheme. Next, we consider the Collins adult brain atlas [20], [21] FEM mesh Version 1 for the THz radiation study. The original brain atlas mesh consists of 70 226 vertices and 423 375 tetrahedral cells. Further, the brain atlas mesh contains scalp/skull, CSF, and gray-matter and white-matter regions; see Fig. 1. The properties of the same were obtained from the literature [12], [22], [23] that were used in the model and are listed in Table I. Next, we consider a breast mesh generated using MR images [24], consisting of 31 910 vertices and 173 101 tetrahedral cells. The fat and fibrous regions of the breast mesh are shown in Fig. 2. Similar to the brain tissue, the breast tissue model properties are given in Table I.

III. RESULTS

A. Comparison of Analytical and Steady-State FEM solution

To validate the FE scheme, we first solve Kirchoff's (steady-state) heat equation, and compare the numerical solution with the analytical solution provided in [15]. A THz beam of radius $a = 0.25$ mm with the power $P = 1$ mW is transmitted at the origin $(0, 0, 0)$. The numerically obtained change in the temperature at $z = 0$ plane as a function of radial distance is plotted in Fig. 3(a). The FE solution is in good agreement with the analytical solution; see Fig. 3(a). Next, the temperature change from the origin $(0, 0)$ with varying height (thickness) z is plotted in Fig. 3(b). Here, the numerical solution coincides with an analytical solution up to the thickness, say $z = 1$ mm, where the mesh is very fine in this region. In comparison with the analytical solution, the numerical solution varies slightly when the thickness increases. Since the mesh becomes very coarser when the thickness increases (the effect of mesh size is studied separately), this could be the reason for the variation in a numerical solution. Nevertheless, we obtain the similar behavior in the numerical solution as compared to analytical solution.

B. Effect of Mesh Size on the Steady-State FEM solution

The FE mesh size (number of vertices/elements) is known to impact the accuracy of the solution especially in the area of illumination [25]. The mesh size indicates the spatial discretization of the tissue under investigation and is important to consider for knowing the accuracy of the computed solution. For this study, we have considered the steady-state case of the heat conduction equation and used it on the brain model with varying nodal density. Due to the diffraction limit, it is hard to focus the THz beam down to spot radius of smaller than 0.25 mm [14], which is considered here as the worst case with the power $P = 1$ mW. Fig. 4 shows the obtained solutions in the region of interest (ROI) with decreasing mesh size (a number of vertices are given at the bottom of each distribution), which clearly indicates that the model having smaller mesh size (more vertices) gave a more stable solution. Note that an increase in the number of vertices beyond 666 999 did not result in significant change in the computed temperature. These meshes with varying spatial discretization were obtained as follows: the mesh with 70 226 vertices is the original Collins adult brain atlas, the mesh with 82 176 vertices is obtained by refining the surface mesh near the ROI and adapted the tetrahedron cells accordingly, whereas the meshes with 567 284 and 666 999 vertices are obtained by uniform refinement of the original mesh and the adaptive mesh, respectively. The discrepancy in the computed temperatures is primarily due to the coarseness of the mesh to model the source (3) accurately; as the distance between the nodes is less than or equal to spot diameter (which is the case for the last column of Fig. 4), the solutions showed no significant numerical errors. Also, the variation in the computed temperatures was not much when this study was repeated for breast mesh indicating that the original breast mesh has sufficient spatial discretization. Note that in cases where the spot radius is greater than 1 mm, the original mesh (first column) itself provided enough robustness to the numerical solution as the nodal distance was at least equal to the spot diameter.
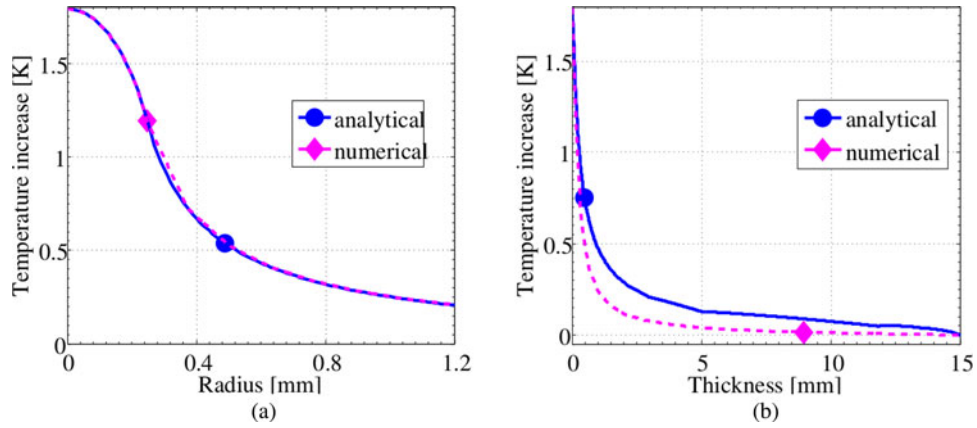
Fig. 3. Comparison of a steady-state solution using the analytical model [15] and the FEM-based model for a cylindrical domain. The variations in (a) radial and (b) axial directions are plotted with temperature raise as the parameter.
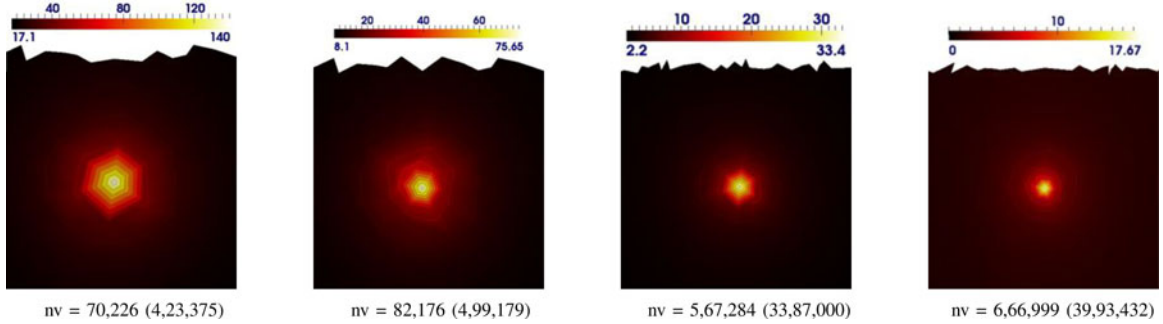

Fig. 4. Mesh size-dependent behavior of temperature raise in the ROI (60 mm × 60 mm centered around the source, shown in Fig. 1) in the brain model using the steady-state equation. The number of vertices (nv) of the FE mesh in each case is given at the bottom of each figure; the corresponding tetrahedral elements are indicated in parenthesis. The input parameters for the model are given in Table I with THz beam radius $a = 0.25$ mm with the power $P = 1$ mW.
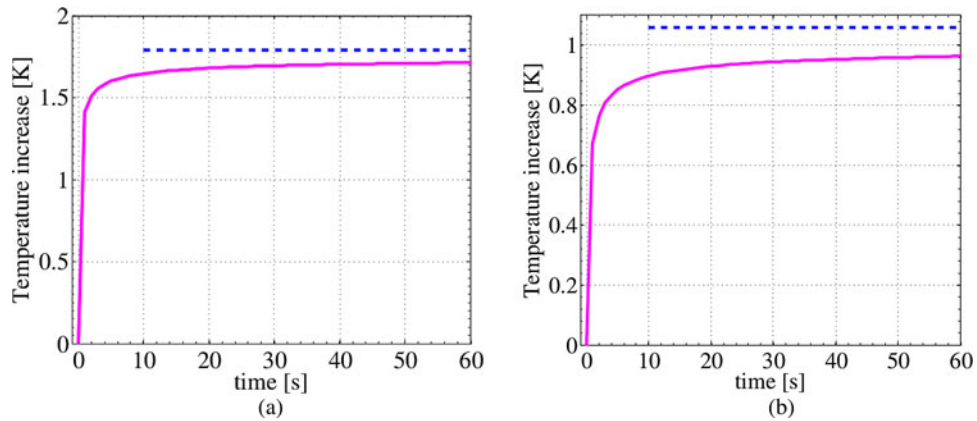

Fig. 5. Time-dependent solutions for a cylindrical domain using the FEM at (a) source location and (b) 0.28 mm along the radial direction for first 1 min. The dashed line indicates the steady-state solution. The THz beam radius is $a = 0.25$ mm and power $P = 1$ mW.

C. Time-Dependent FEM Solutions

Cylindrical Domain: Next, we solve the time-dependent heat conduction equation (2) in the cylindrical domain with the same input parameters as in the aforementioned steady-state case. We use a uniform time step $\triangle t = 0.01$ section in all computations.

The time-dependent behavior of the solution for this case is depicted in Fig. 5 using two test points. The dashed horizontal line in Fig. 5 shows the steady-state solution for comparison. As the time progresses, the transient behavior of the temperature raise slowly decreases and reaches the steady-state solution.
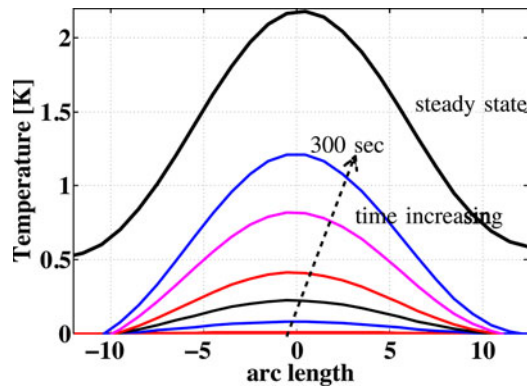
Fig. 6. 1-D plot showing the time-dependent behavior of temperature raise around the source (arc length = 0) in the brain model. The time points that were shown here correspond to 0.5, 1, 10, 30, 60, 150, and 300 s along with a steady-state solution. The input parameters for the model are given in Table I with THz beam radius $a = 2$ mm with the power $P = 1$ mW.

Fig. 8. 1-D plot showing the time-dependent behavior of temperature raise around the source (arc length = 0) in the breast model. The time points that were shown here correspond to 0.5, 1, 10, 30, 60, 150, and 300 s along with a steady-state solution. The input parameters for the model are given in Table I with THz beam radius $a = 0.5$ mm with the power $P = 17$ mW.
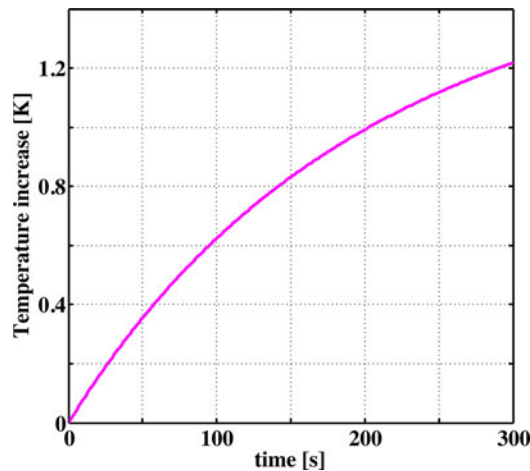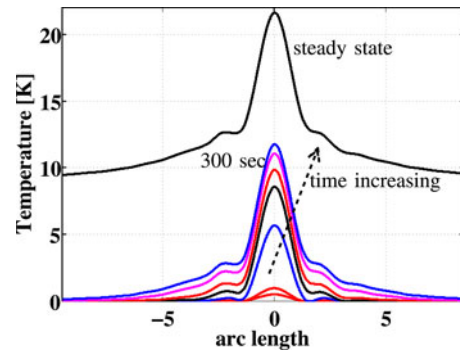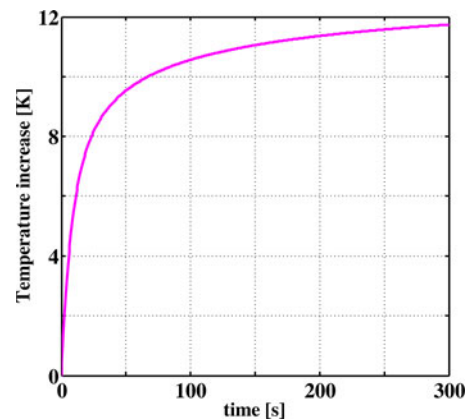

Fig. 7. Transient behavior of temperature raise at the source location corresponding to Fig. 6.

Fig. 9. Transient behavior of temperature raise at the source location corresponding to Fig. 8.

D. Brain Tissue

For the case of realistic tissues, the source radius was different compared to the cylindrical domain case. In the cylindrical domain case, a uniform THz beam profile is used to reproduce the numerical experimental conditions performed in [15]. In this case, a beam of radius 2 mm is used for the THz source with a power of 1 mW along with original brain atlas mesh. The transient behavior of the solution is given in Fig. 6 around the source (as given in Fig. 1) at chosen time points. The steady-state solution in this case is given along with these for effective comparison. 1-D plot of the transient temperature behavior at the source location for this case is shown in Fig. 7. The transient behavior is similar to the trend observed in a cylindrical case (see Fig. 5) except that the time required for reaching the steady state in this case is much greater.

E. Breast Tissue

The source here was also modeled similar to the brain case except that a beam radius was 0.5 mm and power 17 mW. This case actually considers the worst case scenario in terms

of using a modern THz source [8]. The transient behavior of the temperature raise is given in Figs. 8 and 9. Similar to an earlier case, the temperature raise that was observed in this case is much higher compared to brain tissue (see Figs. 6 and 7), as the THz source power is higher and the beam radius is smaller, but the transient behavior (trend) to reach the steady state is similar.

F. Effect of the THz Spot Radius

As mentioned earlier, it is hard to focus the THz beam spot radius below 0.25 mm [14], which forms the worst case scenario. To effectively study the temperature raise as a function of spot radius, we have considered the breast tissue (as the nodal distance in this case was around 0.5 mm) with the power of THz source as 17 mW similar to earlier case. The spot radius was chosen to be 0.25, 1, 2.5, and 5 mm and the observed temperature raise in the ROI is given in Fig. 10 at $t = 60$ s and the steady-state case. The beam spot radius being 0.5-mm result is already presented in Fig. 8. The time point choice of 1 min (top row of Fig. 10) indicates worst case exposure time for a typical THz biomedical application. The results indicate that the raise in the temperature could be as high as 39 °K for the THz exposure of 1 min using the modern sources for the worst case
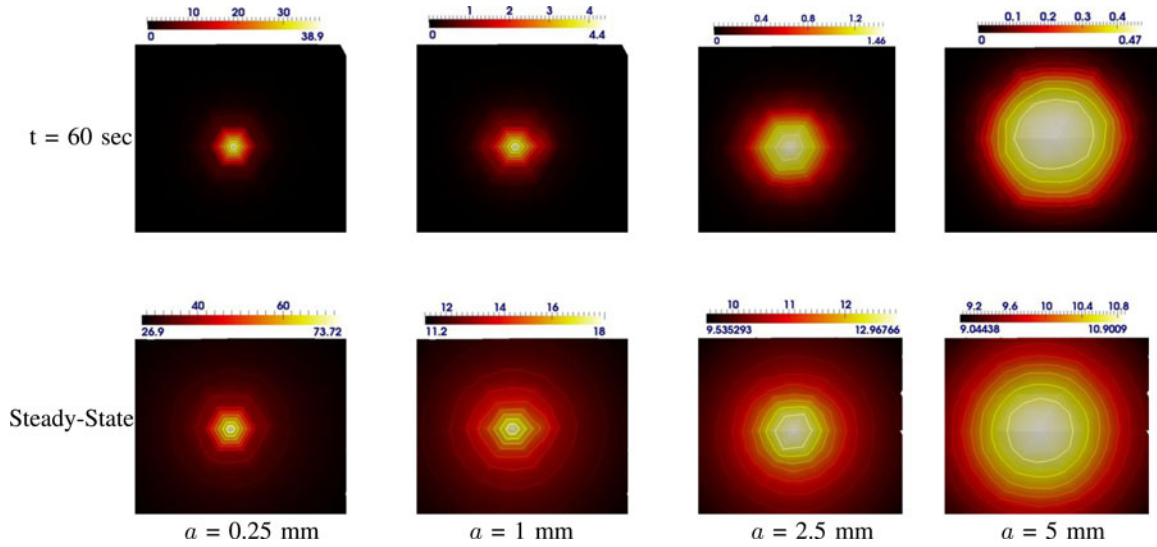
Fig. 10.   THz beam spot radius (a)-dependent behavior of temperature raise in the ROI (12 mm $\times$ 12 mm centered around the source, shown in Fig. 2) in the case of a breast model. The power of the THz source is assumed to be $P = 17$ mW. The top row shows the temperature raise for the exposure time being 60 s and the corresponding steady-state solution is given at the bottom row.

of beam spot radius being 0.25 mm. The beam spot radius of 2.5 mm could be considered as the most practical case, which shows the temperature raise of 1.5 °K.

IV. DISCUSSION

Typical safety limits on the heating effects caused by electro-magnetic radiation are expressed in terms of specific absorption rate (SAR). The SAR in these studies is determined by the for-mulations used in hyperthermia areas [26] and is defined as [12]

$$\text{SAR} = \frac{c_p \triangle T}{\triangle t} \qquad (6)$$

with $\triangle T$ indicating the increase in the temperature observed during time $\triangle t$. Also as specific heat c_p is a inherent property of tissue type, the SAR varies accordingly, leading to different safety limits based on the tissue type. Even though the deter-mination of safety limits is beyond the scope of this study, but SAR values could be easily determined from the developed methodology. Determination of such SAR values is very crit-ical in planning any experiments involving biological tissues. Methodologies that were developed here give a tool for such computations. Also note that from (6), it is evident that SAR is directly proportional to temperature raise in a tissue type and the exposure levels correspond to raise in maximum temperatures, which is determined for the two realistic cases discussed here.

Note that computations performed here represent the worst case scenario, wherein the heat exchange mechanisms (convec-tion and radiation) are excluded in the numerical model, which might be necessary in determining the exact value of highest thermal load. Such determination requires both THz and ther-mal simulations. When the THz propagation problem is well defined in terms of geometry, radiating structure, power level, etc., and does not vary, the temperature raise could be calculated by considering only heat conduction [12].

The obtained steady-state behavior using the same inputs as given in [15] from the FEM technique as observed in Fig. 3 in both radial and axial directions showed that the model that is applied in this work correlates very well with the earlier reported values. The discrepancy in the raise in temperature in the axial direction for the FEM case is primarily due to the coarser nature of mesh in this direction. This discrepancy could be reduced further, if a finer mesh is used with a caveat that the computational complexity in these cases will be much higher. Note that temperature profiles shown in this study have been limited to the ROI for better clarity/presentation as the raise in the temperature is highly localized.

In the FEM scheme, piecewise linear finite elements and a backward Euler method are used for the spatial and tem-poral discretizations, respectively. These discretizations pro-vide first-order convergence in both space and time. In or-der to increase the spatial convergence rate and reduce the numerical error (spatial), higher order finite elements could be used. However, it will increase the computational cost. Alternatively, we could also use an adaptive FE mesh to further reduce the numerical error. The main aim of the study is to compute the maximum raise in temperature in a given model; the convergence studies along with techniques that reduce the numerical error were not taken up in this study.

The numerical accuracy of the solutions presented here highly depends on the mesh size (number of vertices) and THz beam spot radius. Cases where the nodal distance is greater than the beam spot diameter were shown to give erroneous results due to source modeling problems. Decreasing the nodal distance uniformly throughout the mesh, in turn increasing the number of vertices, increases computational complexity and requires more powerful computational setup to achieve the desired accuracy. The better solution is to perform adaptive meshing, where less

nodal distance is chosen in the heating zone resulting in fine mesh in ROI and more coarser mesh elsewhere. Such a choice can be achieved by means of convergence and sensitivity tests, which is beyond the scope of this study and will be taken up as a future extension to this study.

The temperature raise depicted in the realistic tissue case that was considered here has been dealt with sources being placed at only one location and assuming that only one source is illuminated at a time. In a THz tomography setup [27], it might be likely that more than one source might be active. As observed from the results here, the heat raise tends to be highly localized around the source point, making the modeling performed in this study valid for the tomography equipment as well.

As pointed out in [15], the temperature raise observed through modeling is highly dependent on beam width. The temperature raise for a narrower beam is higher and becomes more localized compared to wider THz beams. For narrower beam radius, the temperature raise could be as high as 39 $^{\circ}$K with 1 min exposure, asserting that this could permanently damage the tissue under investigation. Among the brain and breast cases, it is observed here that the temperature raise in brain is comparatively higher (maximum temperature raise of 1.2 $^{\circ}$K to 0.24 $^{\circ}$K with the THz beam spot radius being 2 mm and power being 1 mW) due to the presence of CSF layer in the brain. This also asserts that the temperature effects of the THZ radiation are going to be nonuniform throughout the body, in case where THz will be used in *in vivo* scenario.

The computation time associated with each of these models for a time step was less than 1 s with eight processors, as the linear system of equations solved at each time step is sparse, symmetric, and positive definite. The computational complexity could be further reduced with the deployment of more processors. The memory usage in all these computations is dependent on the FE mesh size, typically the band-width optimized ones providing better computational efficiency.

V. Conclusion

The THz applications are gaining momentum in both biological and defense areas, where the current emphasis is on making them as noninvasive procedures. The planning/setting up of experiments using the biological tissues should have consideration toward safety limits. The finite element-based methodology here can provide the worst case scenario estimations of temperature raise in tissue types, giving immense flexibility toward modeling irregular and inhomogeneous tissue types. The investigation here also revealed that the heating effects are not uniform for all tissues and mainly dependent on the constituents of tissues. The methodologies here assumed that THz radiation will be employed in *in vivo* scenarios, where the real-time measurement of temperature is not possible always and only models could be employed to estimate the temperature raise and provide specific absorption rate towards knowing the safety limits.

References

[1] E. P. J. Parrott, Y. Sun, and E. Pickwell-MacPherson, "Terahertz spectroscopy: Its future role in medical diagnoses," *J. Mol. Struct.*, vol. 1006, no. 1–3, pp. 66–76, 2011.

[2] A. J. Fitzgerald, V. P. Wallace, M. Jimenez-Linan, L. Bobrow, R. J. Pye, A. D. Purushotham, and D. D. Arnone, "Terahertz pulsed imaging of human breast tumors," *Radiology*, vol. 239, no. 2, pp. 533–540, 2006.

[3] P. C. Ashworth, E. Pickwell-MacPherson, E. Provenzano, S. E. Pinder, A. D. Purushotham, M. Pepper, and V. P. Wallace, "Terahertz pulsed spectroscopy of freshly excised human breast cancer," *Opt. Express*, vol. 17, pp. 12444–12454, 2009.

[4] E. Pickwell, A. J. Fitzgerald, B. E. Cole, P. F. Taday, R. J. Pye, T. Ha, M. Pepper, and V. P. Wallace, "Simulating the response of terahertz radiation to basal cell carcinoma using ex vivo spectroscopy measurements," *J. Biomed. Opt.*, vol. 10, no. 6, pp. 064021–064027, 2005.

[5] D. Crawley, C. Longbottom, V. P. Wallace, B. Cole, D. Arnone, and M. Pepper, "Three-dimensional terahertz pulse imaging of dental tissue," *J. Biomed. Opt.*, vol. 8, no. 2, pp. 303–307, 2003.

[6] D. Abbott and X. C. Zhang, "Scanning the issue: T-ray imaging, sensing, and detection," *Proc. IEEE*, vol. 95, no. 8, pp. 1509–1513, Aug. 2007.

[7] R. Appleby and H. B. Wallace, "Standoff detection of weapons and contraband in the 100 GHz to 1 THz region," *IEEE Trans. Antennas Propag.*, vol. 55, no. 11, pp. 2944–2956, Nov. 2007.

[8] C. Worral, J. Alton, M. Houghton, S. Barbieri, H. E. Beere, D. Ritchie, and C. Sirtori, "Continuous wave operation of a superlattice quantum cascade laser emitting at 2 THz," *Opt. Express*, vol. 14, pp. 171–181, 2006.

[9] Y.-S Lee, *Principles of Terahertz Science and Technology*. New York: Springer, 2009.

[10] G. L. Carr, M. C. Martin, W. R. McKinney, K. Jordan, G. R. Neil, and G. P. Williams, "High-power terahertz radiation from relativistic electrons," *Nature*, vol. 420, pp. 153–156, 2002.

[11] M. Sherwin, "Terahertz power," *Nature*, vol. 420, pp. 131–132, 2002.

[12] T. Samaras, P. Regli, and N. Kuster, "Electromagnetic and heat transfer computations for non-ionizing radiation dosimetry," *Phys. Med. Biol.*, vol. 45, pp. 2233–2246, 2000.

[13] A. G. Markelz, "Terahertz dielectric sensitivity to biomolecular structure and function," *IEEE J. Sel. Topics Quantum Electron.*, vol. 14, no. 1, pp. 180–190, Jan.–Feb. 2008.

[14] E. Berry, G. C. Walker, A. J. Fitzgerald, N. N. ZinovÕev, M. Chamberlain, S. W. Smye, R. E. Miles, and M. A. Smith, "Do in vivo terahertz imaging systems comply with safety guidelines," *J. Laser Appl.*, vol. 15, pp. 192–198, 2003.

[15] T. T. L. Kristensen, W. Withayachumnankul, P. U. Jepsen, and D. Abbott, "Modeling terahertz heating effects on water," *Opt. Express*, vol. 18, pp. 4727–4739, 2010.

[16] V. Thomee, *Galerkin Finite Element Methods for Parabolic Problems*, 2nd ed. New York: Springer, 2006.

[17] G. Karypis and V. Kumar, "A fast and highly quality multilevel scheme for partitioning irregular graphs," *SIAM J. Sci. Comput.*, vol. 20, no. 1, pp. 359–392, 1999.

[18] P. R. Amestoy, I. S. Duff, J. Koster, and J.-Y. L'Excellent, "A fully asynchronous multifrontal solver using distributed dynamic scheduling," *SIAM J. Math. Anal. Appl.*, vol. 23, pp. 15–41, 2001.

[19] H. Si, (2012, Mar. 31). "TetGen: A auality tetrahedral mesh generator and a 3D delaunay triangulator," [online]. Available:http://tetgen.berlios.de/.

[20] D. L. Collins, A. P. Zijdenbos, V. Kollokian, J. G. Sled, N. J. Kabani, C. J. Holmes, and A. C. Evans, "Design and construction of a realistic digital brain phantom," *IEEE Trans. Med. Imaging*, vol. 17, no. 3, pp. 463–468, Jun. 1998.

[21] Q. Fang, "Mesh-based Monte Carlo method using fast ray-tracing in Plucker coordinates," *Biomed. Opt. Express*, vol. 1, no. 1, pp. 165–175, 2010.

[22] W. F. Cheong, S. A. Prahl, and A. J. Welsh, "A review of the optical properties of biological tissues," *IEEE J. Quantum Electron.*, vol. 26, pp. 2166–2185, Dec. 1990.

[23] J. Xu, K. W. Plaxco, and S. J. Allen, "Absorption spectra of liquid water and aqueous buffers between 0.3 and 3.72 THz," *J. Chem. Phys.*, vol. 124, pp. 1–3, 2006.

[24] C. M. Carpenter, S. Srinivasan, B. W. Pogue, and K. D. Paulsen, "Methodology development for three-dimensional MR-guided near infrared spectroscopy of breast tumors," *Opt. Express*, vol. 16, pp. 17903–17914, 2008.

[25] E. J. Berjano, "Theoretical modeling for radiofrequency ablation: State-of-the-art and challenges for the future," *Biomed. Eng. Online,*, vol. 5, no. 24, pp. 1–17, 2006.

[26] R. B. Roeme, "Engineering aspects of hyperthermia therapy," *Ann. Rev. Biomed. Eng.*, vol. 1, pp. 347–376, 1999.

[27] S. Wang and X.-C. Zhang, "Pulsed Terahertz tomography," *J. Phys. D, Appl. Phys.*, vol. 37, pp. R1–R36, 2004.

Phaneendra K. Yalavarthy received the M.Sc. degree in engineering from the Indian Institute of Science, Bangalore, India, and the Ph.D. degree in biomedical computation from Dartmouth College, Hanover, NH, in 2004 and 2007, respectively.

He is an Assistant Professor in the Supercomputer Education and Research Centre, Indian Institute of Science, Bangalore. His research interests include medical image computing, medical image analysis, and biomedical optics.

Sashikumaar Ganesan received the Dr.rer.nat degree from Oto-von-Guericke University, Magdeburg, Germany, in 2006 and the M.Sc. degree from Bharathidasan University, Tiruchirappalli, Tamil Nadu, India, both in mathematics.

He is an Assistant Professor in the Supercomputer Education and Research Centre, Indian Institute of Science, Bangalore, India. His research interests include FE analysis and parallel algorithms.